

Predictive 3D modelling of free oblique cutting of Ti6Al4V titanium alloy and experimental validation for a wide range of conditions

[FD:] Include AI?

F. Ducobu^{a,*}, O. Pantalé^b, B. Lauwers^c

^a*Machine Design and Production Engineering Lab, Research Institute for Science and Material Engineering, UMONS, Belgium*

^b*Laboratoire Génie de Production, INP/ENIT, Université de Toulouse, Tarbes, France*

^c*Department of Mechanical Engineering, KU Leuven & Flanders Make@KU Leuven-MaPS, Belgium*

Abstract

Modelling of the cutting process needs to move from a 2D to a 3D configuration to get closer to industrial applications. The study introduces a predictive 3D finite element model of free orthogonal and oblique cutting with an ANN-based material constitutive model and experimental validation in strictly the same conditions (cutting and geometrical). Predictive performance of the model is high for the forces in the 3 directions and the chip thickness ratio on all 36 cutting conditions (including 2 inclination angles). Accuracy of the main cutting force is excellent: the mean difference with the experiments is 3%.

[FD:] Review and update

Keywords:

Oblique cutting, Finite element method (FEM), Predictive model, Artificial Neural Network (ANN)

1. Introduction

2 Selection of the tools and the cutting conditions in machining, but also com-
3 prehension of the influence of the process parameters on the quality of a compo-

*Corresponding author. Tel.: +32 65 45 68

Email address: Francois.Ducobu@umons.ac.be (F. Ducobu)

4 nent and its optimisation, are still difficult to achieve because of the high level
5 of complexity and linked nonlinear phenomena. In the frame of digital manu-
6 facturing and Industry 4.0, modelling of the cutting process supports them, while
7 remaining a challenging task. As highlighted by Arrazola et al. [1], most finite el-
8 ement (FE) models are developed in 2D (orthogonal cutting configuration usually)
9 although industrial applications require a 3D modelling.

10 Experimental validation of a model is a crucial step in the modelling of the
11 cutting process. The experimental configuration must be as close as possible to
12 the simulation. For orthogonal cutting validation, a rotating movement usually
13 generates the cutting speed. This is often achieved in turning [2] or in milling
14 [3] and the diameter of the rotating part must be large enough to reduce the in-
15 fluence of the curvature on the results. Experimental configurations in strictly
16 orthogonal cutting conditions are less often adopted, for example, in broaching
17 [4] or milling [5, 6] machines. While they remove assumptions linked to the ro-
18 tating cutting movement, they usually allow for lower cutting speeds (except on
19 a dedicated machine, such as in Afrasiabi et al. [7]). Free oblique cutting with a
20 straight cutting edge has not been studied yet: all the efforts have been focussing
21 on orthogonal cutting (mostly for 2D validation).

22 Lagrangian and Eulerian formulations are the most used for FE modelling of
23 the cutting process. Combinations of formulations, such as Arbitrary Lagrangian-
24 Eulerian (ALE) and Coupled Eulerian-Lagrangian (CEL) are increasingly used to
25 avoid (or reduce) mesh distortions [8]. The Coupled Eulerian-Lagrangian (CEL)
26 formulation has recently been successfully applied to the modelling of cutting (2D
27 orthogonal configuration): it provides accurate results with a realistic chip shape
28 and no mesh distortion [8]. First applications in 3D are found in recent works
29 [3, 9–12]. They cover (free) orthogonal cutting or a simple 3D operation, while
30 free oblique cutting still needs to be investigated.

The behaviour of the machined material is one of the key aspects of a FE model
[1, 13]. Research is very intense in this field, which leads to a growing number
of material constitutive models ranging from empirical to physical models, some
including microstructure effects [13]. The thermo-elasto-viscoplastic empirical
model of Johnson-Cook (JC) [14] is still the most used so far:

$$\sigma^y = \left(A + B \varepsilon^{p^n} \right) \left(1 + C \ln \frac{\dot{\varepsilon}^p}{\dot{\varepsilon}_0^p} \right) \left(1 - \left[\frac{T - T_{\text{room}}}{T_{\text{melt}} - T_{\text{room}}} \right]^m \right) \quad (1)$$

31 The flow stress, σ^y , is a function of the plastic strain, ε^p , of the plastic strain rate,
32 $\dot{\varepsilon}^p$, and of the temperature, T . It is composed of 3 terms describing independently

plastic, viscous and thermal aspects. One of the points in favour of its adoption is the rather limited number of parameters to be identified, 5: A , B , C , m and n . $\dot{\epsilon}_0^p$ is the reference plastic strain rate, while T_{room} and T_{melt} are the room temperature and the melting temperature, respectively. More recent models developed based on it, such as the one of Calamaz et al. [15], increase this number of parameters (for Calamaz's particular model to 9). The better (in theory) description of the behaviour is achieved at the cost of greater complexity of the identification process and of a reduction of the link with the physical meaning of the model.

One issue of material behaviour modelling for cutting simulation is the identification of the model parameters, moreover as the experimental equipment does not allow to reach the high levels of strains, strain rates and temperature of machining [13]. Inverse identification is an alternative, but the uniqueness of the solution is not always guaranteed [1, 13]. The early work of Özel and Altan [16] used the least squares method to inversely identify the input parameters of a FE model. Shrot and Bäker [17] then used the Levenberg–Marquardt algorithm for their identification of the constitutive material parameters. They showed that similar results (cutting forces and chip morphology) could be obtained by different sets of parameters and therefore highlighted the non-uniqueness of the solution of the inverse problem. In addition to the flow stress parameters, Klocke et al. [18] also identified the damage parameters. In more recent works, such as Bosetti et al. [19] and Denkena et al. [20], the approach to tackle the inverse identification problem is moving from optimisation to Artificial Intelligence (AI) based methods. The Downhill Simplex Algorithm (DSA) is adopted by Bergs et al. [21] and by Hardt et al. [22] for AISI 1045. Stampfer et al. [23] also selected the DSA when dealing with AISI 4140 tempered at 3 different temperatures. In [24], Hardt et al. showed that the Particle Swarm Optimization (PSO) was more efficient to solve the inverse problem than the Downhill Simplex Algorithm, even if computation time is still significant. In an effort to reduce it, an Efficient Global Optimization (EGO) algorithm has recently been introduced by Kugalur Palanisamy et al. [25]. They simultaneously identified the parameters of the material constitutive model and of the friction model for Ti6Al4V. Most of these works highlight the non-uniqueness of the identification and they all require the definition of the analytical expression of the constitutive model.

This paper fills the literature gap on oblique cutting by investigating free orthogonal and oblique 3D cutting configurations from both the experimental and the numerical points of view. An Artificial Neural Network (ANN), introduced in Pantalé et al. [26], is implemented in a FE cutting model for the first time instead of the analytical JC law. A broad range of cutting speeds (6), uncut chip

thicknesses (3) and inclination angles (2) resulting in 36 different conditions are considered to demonstrate the predictive ability of the FE model for fundamental variables. The main goals of a predictive model are the accurate modelling of the trends of the results when the conditions change and predicted values in good agreement with the experimental ones (exact values are not looked for due to experimental dispersions). This type of models aims at supporting future choices and developments without the need of experimental data. No assumption is made about the geometry of the machined workpiece in the model (i.e. its width is the same as in the experiments), while keeping computation time relevant for industrial applications. The developments apply to the titanium alloy Ti6Al4V.

2. Experimental setup

A 3-axis GF Mikron VCE 600 Pro milling machine is used to carry out dry free orthogonal and oblique cutting tests on Ti6Al4V (grade 5 annealed at 750°C for 1 h followed by air cooling) with the same kinematics as a shaper. As shown in Figure 1, the tungsten carbide tool (modified LCGN160602-0600-FG, CP500 from SECO) is fixed on a dedicated holder (modified CFHN-06 from SECO) and the sample to be cut is clamped in the spindle (no rotation is allowed during the test). The top of the sample includes 3 ribs of 1 mm in width (width of the tool is 6 mm) and 10 mm in length. The test consists of removing the upper layer (its height is the uncut chip thickness, h) of one rib at the prescribed cutting speed, v_c . The cutting speed is provided by the feed rate, v_f , of the machine (max. value of 40 m/min). The tool cutting edge inclination, λ_s , results from the relative angular orientation of the tool and the sample. Table 1 shows the cutting conditions: 6 cutting speeds, 3 uncut chip thicknesses and 2 inclination angles, each is repeated 3 times.

Forces are measured with a 3-component Kistler 9257B dynamometer and are amplified by a Kistler 5070A charge amplifier. Acquisition is performed at 3 kHz with a Kistler 5697A2 data acquisition system and the DynoWare software. Recorded forces are then filtered with a second-order low-pass Bessel filter at 750 Hz before computing the mean value of the signal at steady state.

All the chips are collected and observed with a Dino Lite digital microscope AM7013MZT (5 MP, magnification 20× – 250×). Each chip is measured 3 times along its length to get a mean value representative of the whole chip.

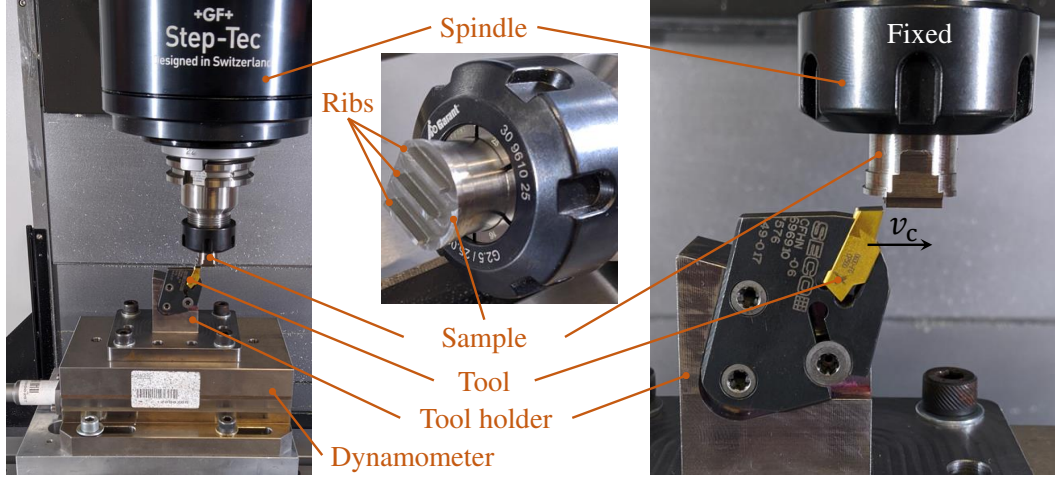


Figure 1: Experimental setup

Table 1: Cutting conditions of the study

Parameter	Values
Cutting speed, v_c (m/min)	5, 7.5, 10, 20, 30, 40
Uncut chip thickness, h (μm)	40, 60, 80
Cutting edge inclination, λ_s ($^\circ$)	0, 6
Width of the workpiece (mm)	1
Length of the workpiece (mm)	10
Width of the cutting edge (mm)	6 (1.1 in the model)
Cutting edge radius, r_β (μm)	20
Rake angle, γ_0 ($^\circ$)	15
Clearance angle, α_0 ($^\circ$)	2

104 3. Finite element model

105 3.1. Modelling choices

106 The CEL formulation is adopted to model the dry free orthogonal and oblique
 107 cutting tests with Abaqus/Explicit 2020. The 3D model is composed of a fixed
 108 Lagrangian tool and a Eulerian workpiece (Figure 2). Chip formation occurs by
 109 plastic flow across the Eulerian domain with no mesh distortion. The Eulerian for-
 110 mulation enables to form chips without damage properties, removing modelling

assumptions. These two characteristics contribute to cutting models providing accurate results and realistic chips [8].

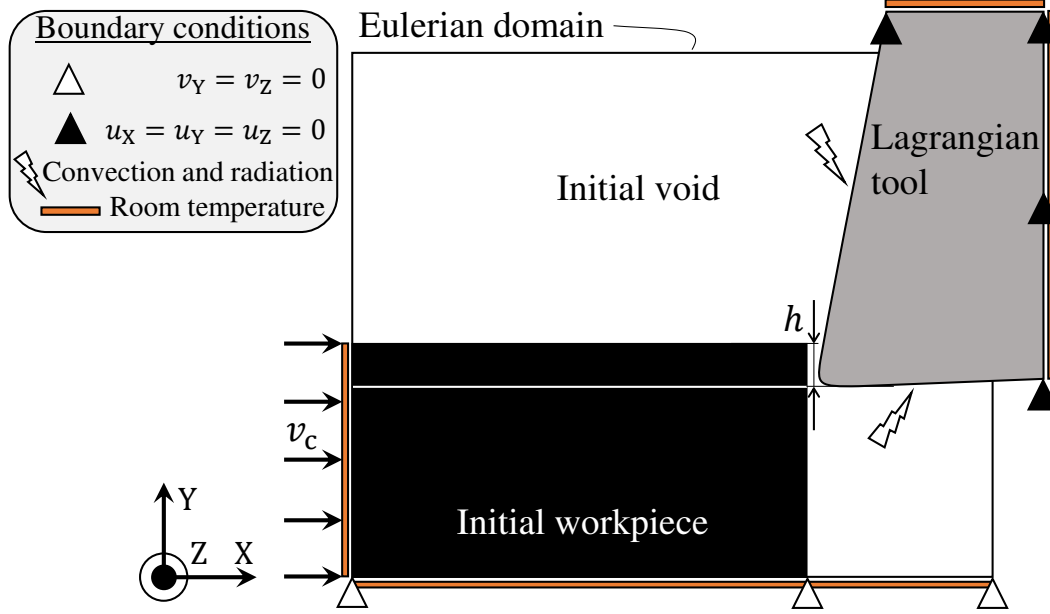


Figure 2: Boundary conditions and schematic initial geometry of the model

As shown in Figure 3, the full width of the workpiece, i.e. a rib in the experiments, (1 mm) is modelled. To allow chip formation and side flow, the Eulerian domain is wider (it includes the volume in which material can move). The volume above the initial workpiece is also meshed with Eulerian elements for the same reasons. As in the experiments and to fulfil the hypothesis of free orthogonal and oblique cutting, the tool is wider than the workpiece (it is of 1.1 mm in the model and of 6 mm in the experiments). It is very important to stress that the models are the same for both inclination angles: they only differ by the rotation of the tool of 6° about Y axis as in the experiments (Figure 3). This, coupled to the absence of assumptions when developing the models, contributes to make the models predictive: no input is changed when cutting conditions do.

According to a previous mesh sensitivity study in orthogonal cutting with the CEL formulation [9], elements edge size is $5\text{ }\mu\text{m}$ in the plane parallel to the cutting speed. In the direction perpendicular to this plane, it is $5\text{ }\mu\text{m}$ in areas close to the lateral boundaries of the Eulerian domain and $50\text{ }\mu\text{m}$ in the middle of the workpiece. To reduce computation time, the size of the model depends on the value of

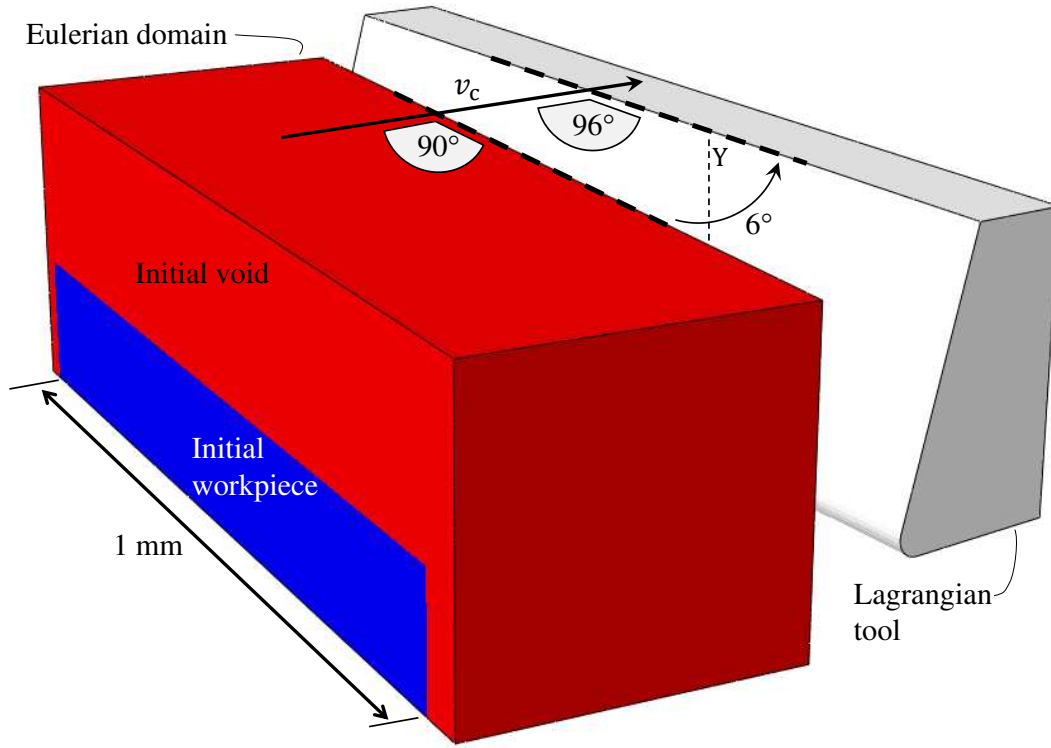


Figure 3: Configuration of the FE model for $\lambda_s = 6^\circ$

the uncut chip thickness. This results in a Eulerian domain (EC3D8RT linear 3D Eulerian elements with 8 nodes, coupled mechanical-thermal behaviour and reduced integration) composed of 216,550 to 273,350 nodes and a Lagrangian domain (C3D8T linear 3D Lagrangian elements with 8 nodes, coupled mechanical-thermal behaviour) of 4,650 nodes.

The Ti6Al4V workpiece is assumed to be thermo-elasto-viscoplastic (isotropic) and inelastic heat fraction is 0.9. JC set of parameters from Seo et al. [27] is adopted as the value of A corresponds to the typical yield stress value of Ti6Al4V and this set proved to provide the best results among 20 sets available in the literature [28]. The tungsten carbide tool with TiN coating is assumed to be linear elastic. Material properties are provided in Table 2.

Following the experimental results of Rech et al. [31], Coulomb's friction is assumed to occur at the tool-workpiece interface and both friction, μ , and heat partition, β , coefficients depend on the cutting speed. Limiting shear stress, τ_{\max} ,

Table 2: Materials properties [27, 29, 30]

Young's modulus, E (GPa)	Ti6Al4V	113.8*
	WC	650
Poisson's ratio, ν	Ti6Al4V	0.34
	WC	0.2
Density, ρ (kg/m ³)	Ti6Al4V	4,430
	WC	14,850
Conductivity, k (W/mK)	Ti6Al4V	6.3*
	WC	100
Expansion, α (K ⁻¹)	Ti6Al4V	8.6 e ⁻⁶ *
	WC	5 e ⁻⁶
Specific heat, c_p (J/KgK)	Ti6Al4V	531*
	WC	202
JC constitutive model	A (MPa)	997.9
	B (MPa)	653.1
	C	0.0198
	m	0.7
	n	0.45
	$\dot{\epsilon}_0$ (s ⁻¹)	1
	T_{room} (K)	293
	T_{melt} (K)	1873

*: Dependence to the temperature, value provided at 293 K

is included and is given by

$$\tau_{\max} = \frac{\text{yield stress}}{\sqrt{3}} = \frac{A}{\sqrt{3}} \quad (2)$$

140 All the friction energy is converted into heat. Table 3 shows the friction coeffi-
141 cients adopted in this study.

142 Room temperature of 293 K is imposed on the upper and right surfaces of the
143 tool and on the left and bottom surfaces of the workpiece (Figure 2). Radiation
144 and convection are assumed to occur on the rake and clearance faces of the tool.
145 Initial temperature of the tool and the workpiece is set to room temperature (293
146 K). Heat transfer coefficients are provided in Table 3.

Table 3: Friction and heat transfer coefficients [29, 31]

Cutting speed, v_c (m/min)	μ	β
5	0.24	1
7.5	0.22	0.89
10	0.21	0.80
20	0.19	0.63
30	0.18	0.55
40	0.17	0.50
Limiting shear stress, τ_{\max} (MPa)	576	
Convection, U (W/m ² K)	50	
Radiation, ϵ	0.3	

147 3.2. Material constitutive model of Ti6Al4V

148 The constitutive model of the Ti6Al4V material used in all the numerical sim-
149 ulations proposed in section 4 is a thermo-elasto-viscoplastic law using a flow cri-
150 terion based on an ANN identified for the selected material and implemented in
151 the Abaqus/Explicit code via a Fortran routine VUHARD as proposed by Pantalé
152 et al. in [26]. The principle of this approach consists in replacing the analyti-
153 cal formulation of the flow law, based on a Johnson-Cook or Zerilli-Armstrong
154 type model, and allowing the calculation of the flow stress σ^y as a function of the
155 plastic strain ε^p , of the plastic strain rate, $\dot{\varepsilon}^p$, and of the temperature T , by a multi-
156 layer ANN serving as universal approximator. Thus, the parameters of the neural
157 network can directly be identified from the experimental data without having to
158 postulate a behavioural model, which simplifies the procedure and allows more
159 flexibility in the definition of the model. The proposed approach also allows, as
160 shown in Pantalé et al. [26], to compute the derivatives of the flow stress σ^y with
161 respect to the three input variables of the model, a necessary step to implement this
162 model as a flow law in the form of a VUHARD subroutine in the Abaqus/Explicit
163 FEM code.

164 In order to verify the influence of the complexity of the neural network on the
165 numerical results of the simulation and the computing time, several architectures
166 of ANN are tested thereafter (in 3.4). The chosen global architecture has 2 hidden
167 layers with a variable number of neurons for the first hidden layer ($\zeta = 9$ to 17)
168 and 7 neurons for the second hidden layer, 3 inputs (plastic strain, ε^p , plastic

169 strain rate, $\dot{\varepsilon}^p$, and temperature, T) and one output (the yield stress, σ^y). The
 170 global architecture of this kind of ANN is given in Figure 4 for 9 neurons in
 171 the first hidden layer. Conforming to Pantalé et al. [26], this ANN is referred
 172 after the terminology ANN 3-9-7-1-sig, because it has 3 inputs, 9 neurons in the
 173 first hidden layer, 7 neurons in the second hidden layer, 1 output and a sigmoid
 174 activation function.

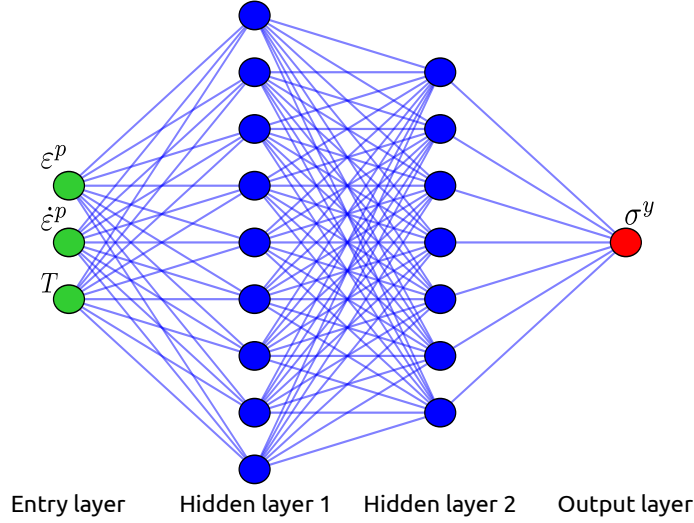


Figure 4: Architecture of the ANN 3-9-7-1-sig used for the flow law

175 The main advantage of this approach (the use of an ANN), after the training
 176 phase, is that the output σ^y of the network is related to the inputs ε^p , $\dot{\varepsilon}^p$, and T
 177 through equations (3) to (7). The first step is to scale the input data to the interval
 178 $[0, 1]$ using the following equation:

$$\vec{x} = \begin{cases} x_1 = \frac{\varepsilon^p - [\varepsilon^p]_{min}}{[\varepsilon^p]_{max} - [\varepsilon^p]_{min}} \\ x_2 = \frac{\ln(\dot{\varepsilon}^p) - [\ln(\dot{\varepsilon}^p)]_{min}}{[\ln(\dot{\varepsilon}^p)]_{max} - [\ln(\dot{\varepsilon}^p)]_{min}} \\ x_3 = \frac{T - [T]_{min}}{[T]_{max} - [T]_{min}} \end{cases} \quad (3)$$

179 The outputs of the neurons in the first hidden layer are given by the following
 180 equation:

$$\vec{y}_1 = \text{sig}(\mathbf{w}_1 \cdot \vec{x} + \vec{b}_1) \quad (4)$$

where, $\text{sig}()$ is the sigmoid activation function defined by equation (5):

$$\text{sig}(x) = \frac{1}{1 + e^{-x}} \quad (5)$$

Then, the output of the neurons in the second hidden layer are given by equation (6):

$$\vec{y}_2 = \text{sig}(\mathbf{w}_2 \cdot \vec{y}_1 + \vec{b}_2) \quad (6)$$

So, the output of the ANN is therefore given by equation (7).

$$\sigma^y = ([\sigma^y]_{max} - [\sigma^y]_{min}) (\vec{w}^T \cdot \vec{y}_2 + b) + [\sigma^y]_{min} \quad (7)$$

181 In equations (3) to (7), quantities \mathbf{w}_1 , \mathbf{w}_2 , \vec{w} , \vec{b}_1 , \vec{b}_2 and b are given by the
 182 training procedure of the ANN. Corresponding values for an ANN containing 9
 183 neurons in the first hidden layer are reported in Appendix A. Quantities $[\]_{min}$ and
 184 $[\]_{max}$ are the boundaries of the range of the corresponding field during the training
 185 phase, values are also given in Appendix A.

186 Because of the large number of identified parameters for all the ANN models
 187 (from 114 to 202 for 9 and 17 neurons for the first hidden layer, respectively);
 188 the other 4 sets of ANN parameters used in this publication can be found in [32].

189 [FD:] Inclure dans corps du texte puisque article normal et rq reviewer?

190 3.3. Sensitivity study of the results to mass scaling

FE modelling of the cutting process is very expensive in CPU computation time because of the coupling fn many nonlinear phenomena and the large amount of tiny finite elements. Mass scaling (MS) is introduced in the model to reduce the CPU computation time while checking that it does not influence the results (forces and energies) via a mass scaling sensitivity study. MS factors, MS_f , ranging from 1E6 (theoretical scaling of CPU time of $\sqrt{MS_f} = 1000$) to 1 (no scaling) have been used for one cutting condition ($\lambda_s = 0^\circ$, $v_c = 30$ m/min and $h = 60$ μm). The same signal processing procedure is applied to the numerical forces as to the experimental forces (cf. 2): they are filtered with a second-order low-pass Bessel filter at 750 Hz before computing the mean value at steady state. Table 4 gives the results normalised (\hat{F}_i) by these of the model without MS:

$$\hat{F}_i = \frac{F_i \text{ with MS}}{F_i \text{ without MS}} \quad (8)$$

191 With $i = c$ for the cutting force and $i = f$ for the feed force. As expected,
 192 actual speed-up does not increase linearly with the MS_f , but it is still significant.

193 MS_f of 1E6 leads to unstable computation and MS_f of 1E5 results in erratic
 194 forces evolutions. These results are confirmed by high values of the kinetic (KE)
 195 on internal (IE) energies ratio (it should not exceed a few % [33, 34]). A MS_f
 196 value of 1E3 is selected as it provides a good balance between computation time
 197 reduction and impact on forces, while keeping $\frac{KE}{IE}$ below 1%. To provide an order
 198 of magnitude of CPU computation time, between 10 h and 50 h (depending on the
 199 value of h) are needed on 4 cores of an Intel i7-5700HQ CPU at 2.7 – 3.5 GHz.

Table 4: MS sensitivity study (selected MS factor, MS_f , in bold, \hat{F}_c : normalized cutting force, \hat{F}_f : normalized feed force, KE : kinetic energy, IE : internal energy)

MS_f	CPU scaling	Speed-up	\hat{F}_c	\hat{F}_f	$\frac{KE}{IE}$ (%)
1	1	1	1	1	2.3E-4
1E2	10	9	1.006	0.982	2.2E-2
1E3	32	21	1.008	0.940	2.2E-1
1E4	100	61	1.012	0.921	2.4
1E5	316	173	Erratic	Erratic	22
1E6	1000	207	Unstable	Unstable	58

200 3.4. Sensitivity study of the results to the number of neurons

The number of neurons on the hidden layers may influence the results. A sensitivity study on the number of neurons for the first hidden layer, ζ , is carried out to select the ANN providing the best balance between CPU computation time and quality of the results. The results of the study are provided in Table 5. \check{F}_i corresponds to the results normalised by these of the model with the built-in JC model:

$$\check{F}_i = \frac{F_i \text{ with ANN}}{F_i \text{ with JC}} \quad (9)$$

201 They show no influence on the forces when compared to the built-in Johnson-
 202 Cook model, only computation time is influenced. A first hidden layer with 9
 203 neurons is therefore selected as it leads to the lowest CPU computation time in-
 204 crease.

205 4. Experimental and numerical results

An example of temporal evolutions of numerical and experimental forces is plotted for the 3 directions in Figure 5 at $\lambda_s = 6^\circ$, $v_c = 10$ m/min and $h = 40$ μ m.

Table 5: Sensitivity of the forces to the number of neurons of the first layer, ζ (selection in bold, \check{F}_c : normalized cutting force, \check{F}_f : normalized feed force)

ζ	Time increase (%)	\check{F}_c	\check{F}_f
Built-in	0	1.000	1.000
9	6	1.000	0.999
11	6	1.001	1.000
13	7	1.000	0.998
15	8	1.001	1.001
17	10	1.000	1.000

Computation of the FE models is carried out until a few microseconds after the steady state is reached. Then, linear extrapolation (dashed line between the two last markers in Figure 5) is used to provide numerical values during the same time range as the experimental values. Mean and standard deviation (2σ) are computed from the 3 experimental values. The resulting dispersion is plotted in Figure 5 around the mean values of each forces. Steady state takes more time to be reached for the experiments than in the numerical model, and particularly for the cutting force. Dispersion around the mean force evolution is larger for the feed force than for the cutting force, while the mean feed force value is 46% of the mean cutting force value. The numerical cutting force is very close to the experimental mean cutting force; it is only 4% larger). This difference is computed by

$$\Delta i = \frac{|i^{(\text{sim})} - i^{(\text{exp})}|}{i^{(\text{exp})}} \times 100 \quad (10)$$

206 The numerical feed force is underestimated by the model, but it is at the bound-
 207 ary of the 95% experimental confidence interval. The numerical passive force
 208 difference is also underestimated, but it is not in the narrower experimental dis-
 209 persion. Difference between the mean values of experimental and numerical feed
 210 and passive forces is 25%. This value for the feed force... + [x] For the passive
 211 force... + [x]

212 Numerical chips at $v_c = 10$ m/min and $h = 40$ μm for $\lambda_s = 0^\circ$ and $\lambda_s = 6^\circ$
 213 are provided in Figures 6 and 7. When the cutting edge inclination is 0° , both
 214 sides of the chip are identical and a symmetry plane can be drawn in the middle
 215 of the workpiece (Figure 7 (a)). On the contrary, for the cutting edge inclination
 216 of 6° , the chip is not aligned with the workpiece anymore. The chip bends on

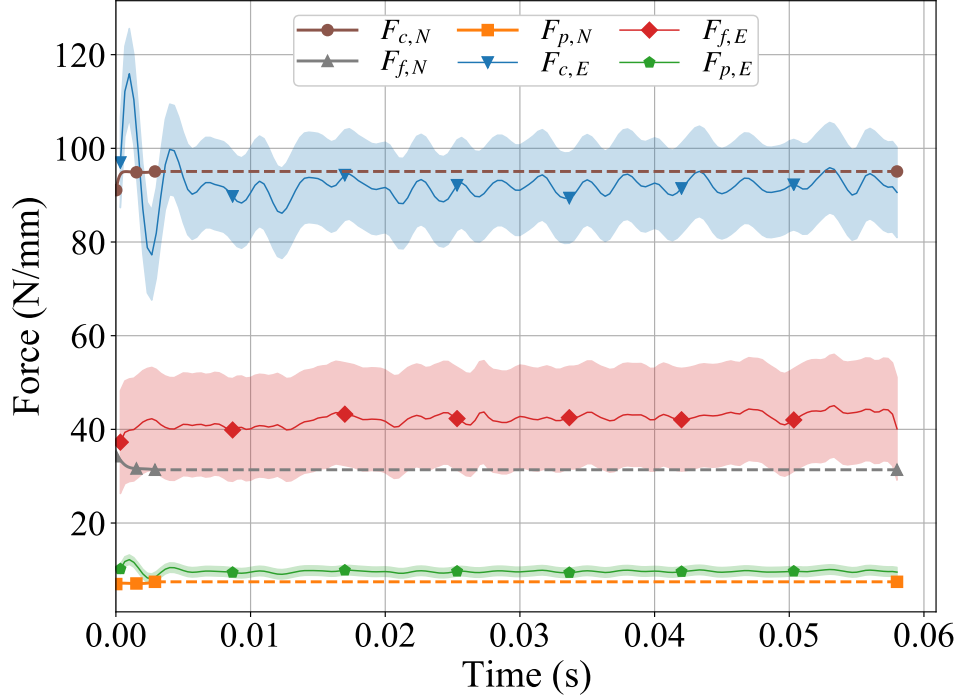


Figure 5: Temporal evolutions of experimental (E) and numerical (N) forces at $\lambda_s = 6^\circ$, $v_c = 10$ m/min and $h = 40 \mu\text{m}$: dispersion around mean experimental values and linear extrapolation of numerical values in dashed

217 one side due to the orientation of the tool and the symmetry is lost for both the
 218 geometry, and the thermal and mechanical fields as highlighted in Figure 7 (b).
 219 This produces helical chips for the inclination angle of 6° as in the experiments.
 220 Figure 8 shows the variation of the chip thickness across its width: it is thicker
 221 in the middle (i.e. the body of the chip) than on its sides. This stresses on the
 222 importance of a 3D modelling, even for the orthogonal cutting configuration as
 223 already highlighted by [?]. 3D modelling also allows to reproduce the side flow
 224 occurring in the experiments for both cutting edge inclination values (Figure 6),
 225 contrary to a 2D model []. Although this leads to higher computation times, future
 226 cutting models should be in 3D, even when orthogonal cutting is considered. In
 227 this case, it is recommended to take advantage of the symmetry of the configu-
 228 ration to reduce computation time. This simplification has not been included in

229 this study to avoid any difference in the FE models between the 2 cutting edge
 230 inclinations.

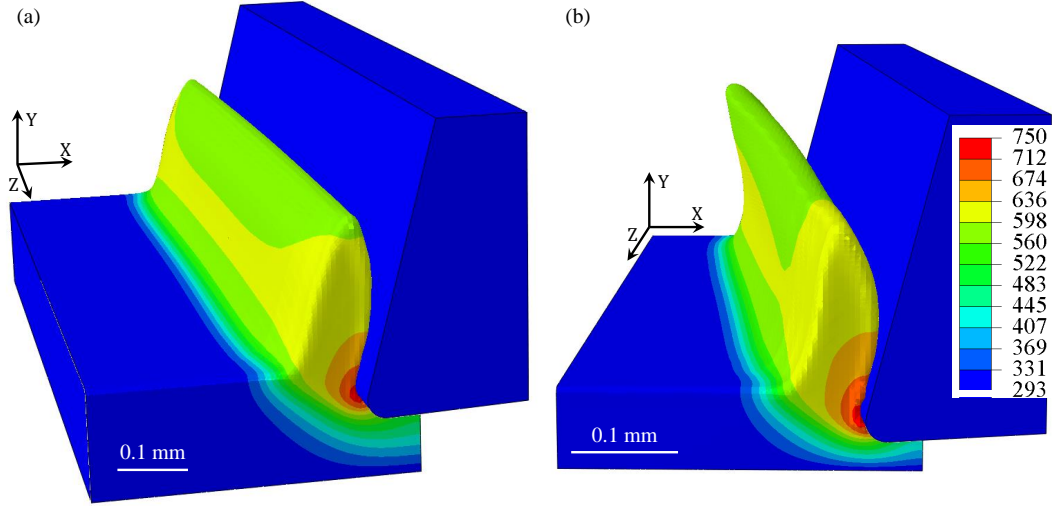


Figure 6: Temperature contours (in K) of the numerical chip after 1.5 ms at $v_c = 10$ m/min, $h = 40$ μ m and (a) $\lambda_s = 0^\circ$ and (b) $\lambda_s = 6^\circ$

231 Mean values of the experimental forces and their dispersion are shown in Fig-
 232 ures 9 to 13 together with the mean numerical values. Passive force values are of
 233 course only plotted for $\lambda_s = 6^\circ$ as they are equal to zero when $\lambda_s = 0^\circ$.

234 The increase of the cutting force with the uncut chip thickness is clearly ob-
 235 served in Figures 9 and 10 for both experimental and numerical results at the 2
 236 inclination angles, as well as the decrease of the force with the increase in the cut-
 237 ting speed. This shows temperature softening domination on strain rate hardening
 238 for Ti6Al4V and that it is accurately modelled. The increase of the inclination
 239 angle from 0° to 6° slightly reduces the cutting force; this is well captured by the
 240 model. For cutting speeds of 20–40 m/min and inclination angle of 0° , F_c is al-
 241 most constant with the cutting speed for uncut chip thicknesses of 40 μ m and 60
 242 μ m, while it slightly decreases for 80 μ m; this small stabilisation is less marked
 243 for the modelling.

244 An increase in the deviation around the mean value with the cutting speed is
 245 noted for values above 10 m/min. All numerical values are within a confidence
 246 interval of 95% of the experiments (35 out of 36 conditions are within a confidence
 247 interval of 68%) and the mean difference with the experiments is 3%, which is
 248 remarkable, moreover given the wide range of cutting conditions considered and

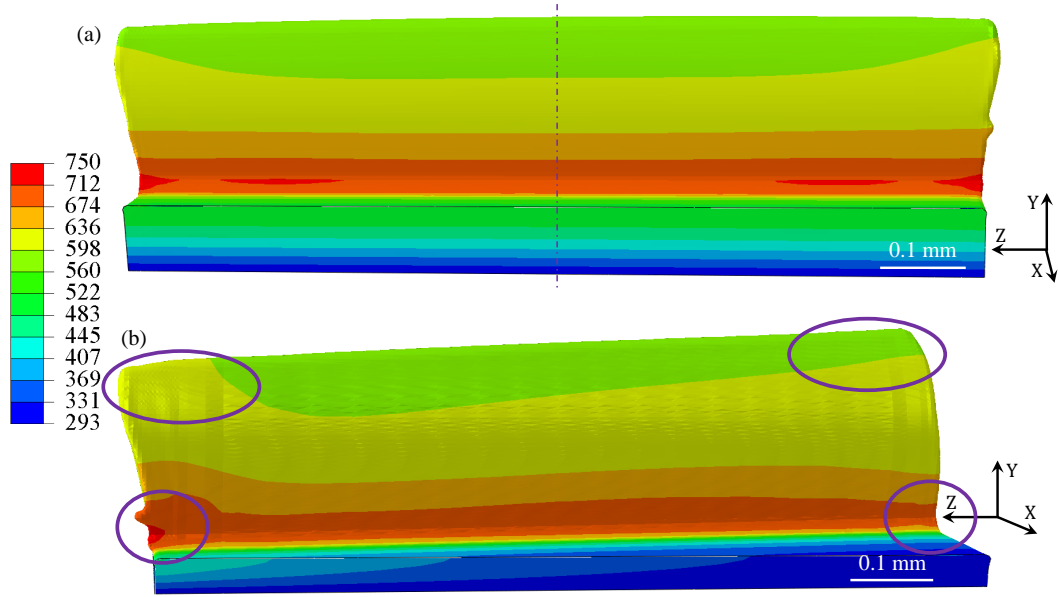


Figure 7: Temperature contours (in K) of the back of the numerical chip (tool is removed) after 1.5 ms at $v_c = 10$ m/min, $h = 40$ μ m and (a) $\lambda_s = 0^\circ$ and (b) $\lambda_s = 6^\circ$

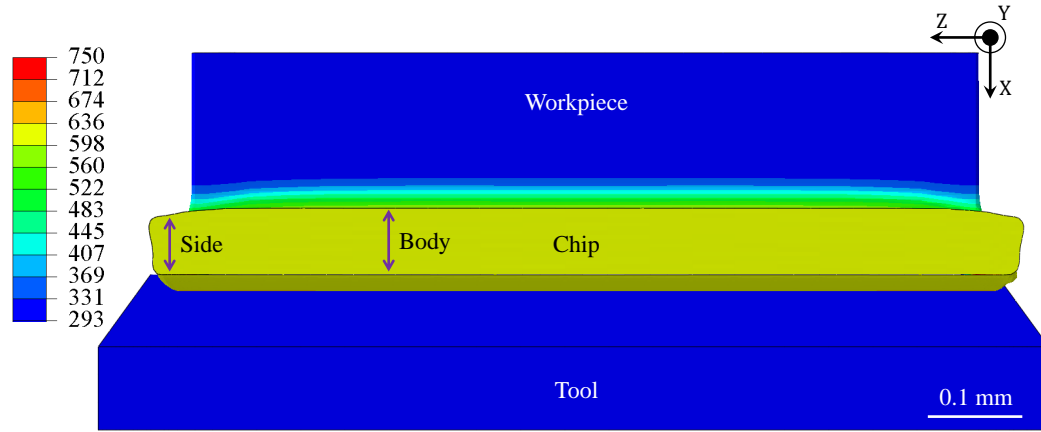


Figure 8: Temperature contours (in K) of the top of the numerical chip after 1.5 ms at $v_c = 10$ m/min, $h = 40$ μ m and $\lambda_s = 0^\circ$

249 the absence of tuning of the model. This highlights the predictive ability of the FE
250 model for both inclination angles.

251 Figures 11 and 12 show the results for the feed force, where the two clearest

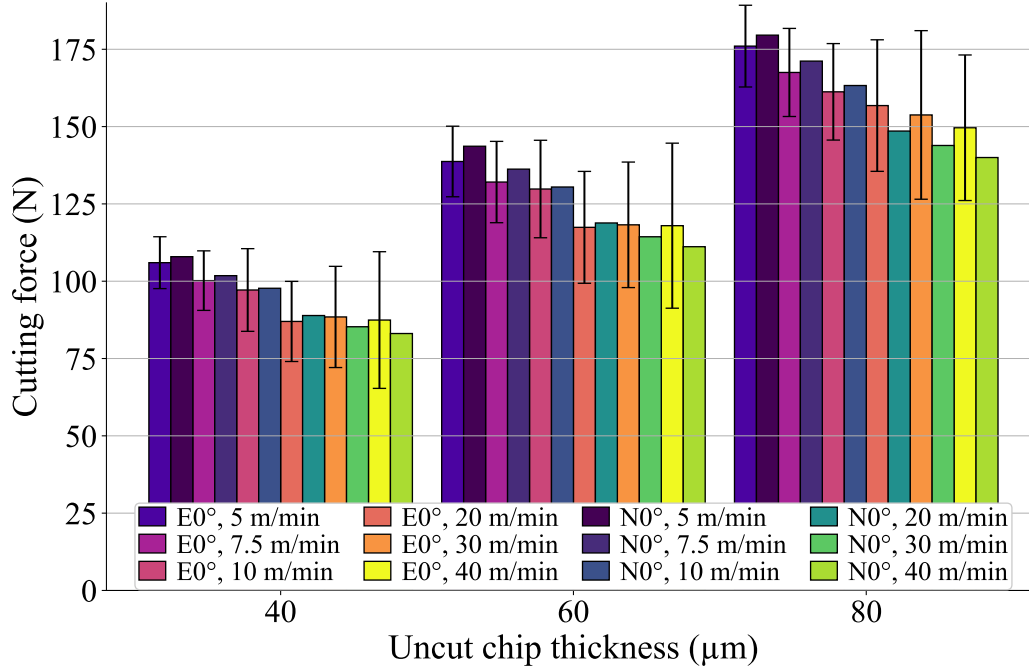


Figure 9: Comparison of experimental (E) and numerical (N) cutting forces at the cutting edge inclination of 0° for the 3 uncut chip thicknesses (40, 60 and 80 μm) and the 6 cutting speeds (5, 7.5, 10, 20, 30 and 40 m/min)

trends for the experiments are its decrease with inclination angle and its increase
 with the uncut chip thickness (even if it is smaller that the expectations). For 80
 μm , F_f globally decreases with v_c in the experiments. For 40 μm and 60 μm , the
 force decreases at lower v_c and then increases for 0° , while a decrease is observed
 at all v_c for 6° . For the numerical values, the global trend is the same for the
 3 uncut chip thicknesses and both inclination angles: a decrease for the lowest
 v_c values and then an increase. It must be noted that the numerical model does
 not handle correctly the feed force trends: as clearly shown by Figure 12, the
 numerical forces have globally an increasing trend with the cutting speed, while
 their mean value mostly decreases when the uncut chip thickness increases. Dif-
 ferences between the mean numerical and experimental values increase with the
 uncut chip thickness: forces are closer at 40 μm than at 80 μm . The numerical
 values are mostly not within the 95% confidence interval (it has no clear evolution
 with the cutting conditions). Coupled with the differences in trends, it shows that
 F_f is less well modelled (mean difference is 35%) than F_c as usual in FE mod-

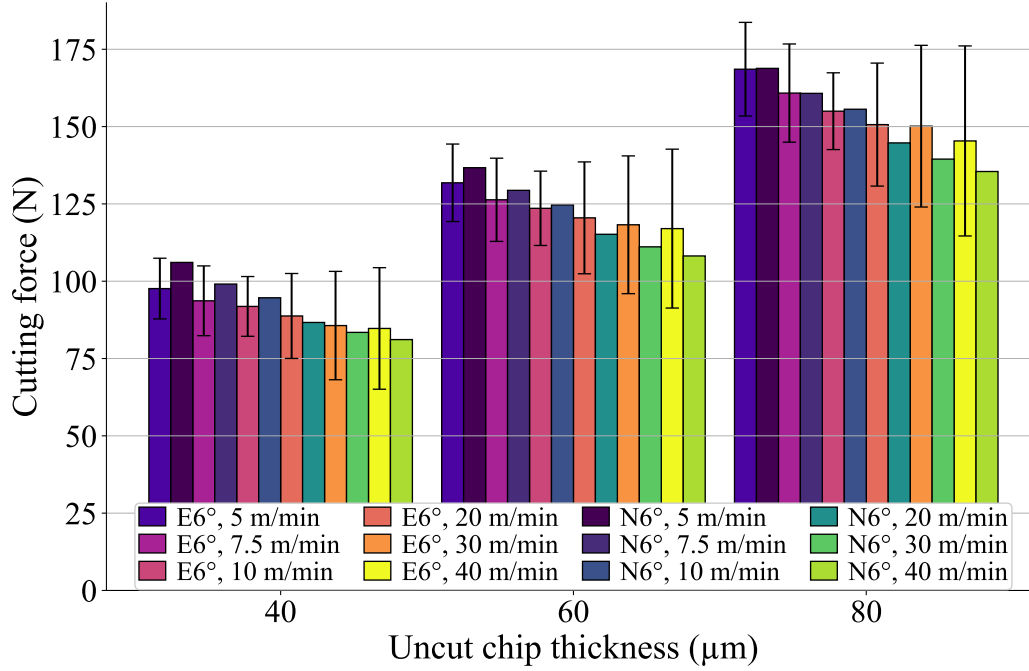


Figure 10: Comparison of experimental (E) and numerical (N) cutting forces at the cutting edge inclination of 6° for the 3 uncut chip thicknesses (40, 60 and 80 μm) and the 6 cutting speeds (5, 7.5, 10, 20, 30 and 40 m/min)

elling of the cutting process []. The influence of the uncut chip thickness on the feed force should therefore be improved. Material constitutive model parameters are known to have an impact on the forces (and on the chip morphology) [?]. The friction model should be improved as well to enhance the results.

Passive force is non-zero for the inclination angle of 6° (Figure 13). As the cutting force, it increases with the uncut chip thickness and it decreases with the cutting speed. Comparison with the experiments is globally the same as for F_c , except for a larger difference in the magnitude of F_p (mean difference is 26%, but it is small in absolute – less than 5 N). The numerical values are mostly not in the 95% experimental confidence interval.

Regarding the chips morphology, all the chips are continuous. For both the simulation and the experiments, the chip thickness ratio, λ_h :

$$\lambda_h = \frac{h'}{h} \quad (11)$$

with h the uncut chip thickness and h' the chip thickness, is almost independent of

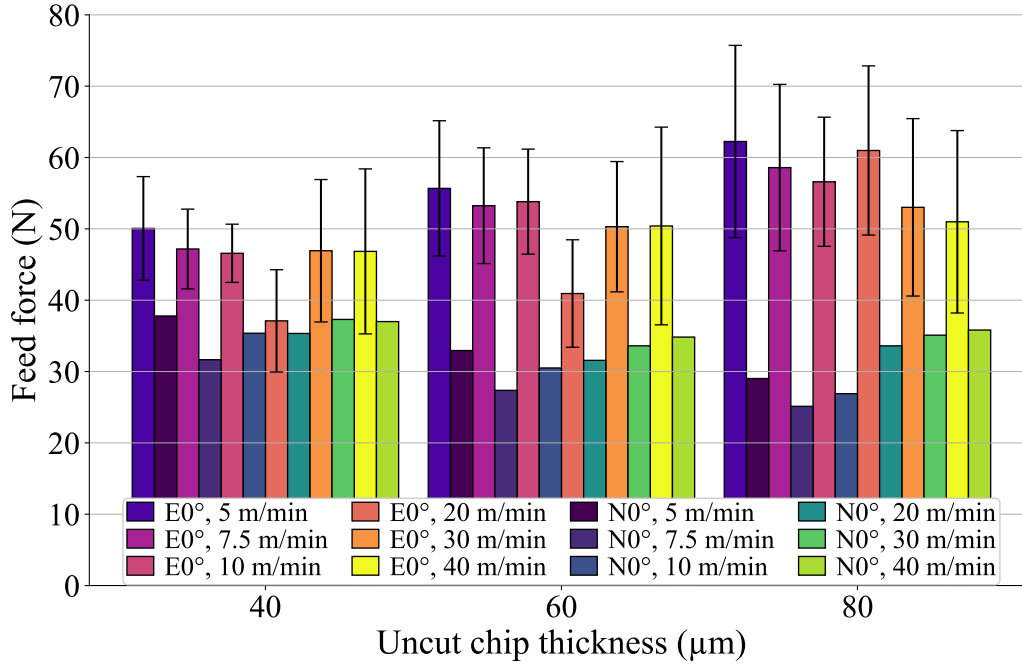


Figure 11: Comparison of experimental (E) and numerical (N) feed forces at the cutting edge inclination of 0° for the 3 uncut chip thicknesses (40, 60 and 80 μm) and the 6 cutting speeds (5, 7.5, 10, 20, 30 and 40 m/min)

the uncut chip thickness. It is slightly reduced from $\lambda_s = 0^\circ$ to $\lambda_s = 6^\circ$, meaning that the chip thickness is reduced with the inclination angle. This influence is underestimated by the model: the reduction of λ_h is lower than in the experiments. The mean difference between experimental and numerical λ_h is 17% across the whole range of cutting conditions. The chip thickness ratio decreases with the cutting speed because of the reduction of friction, which is correctly captured by the model. As for the feed force, the results should be improved by more complex friction models and a set of material constitutive parameters for which the identification includes the forces and the chip thickness [25].

Differences computed according to equation 10 + comment and link to Table 6

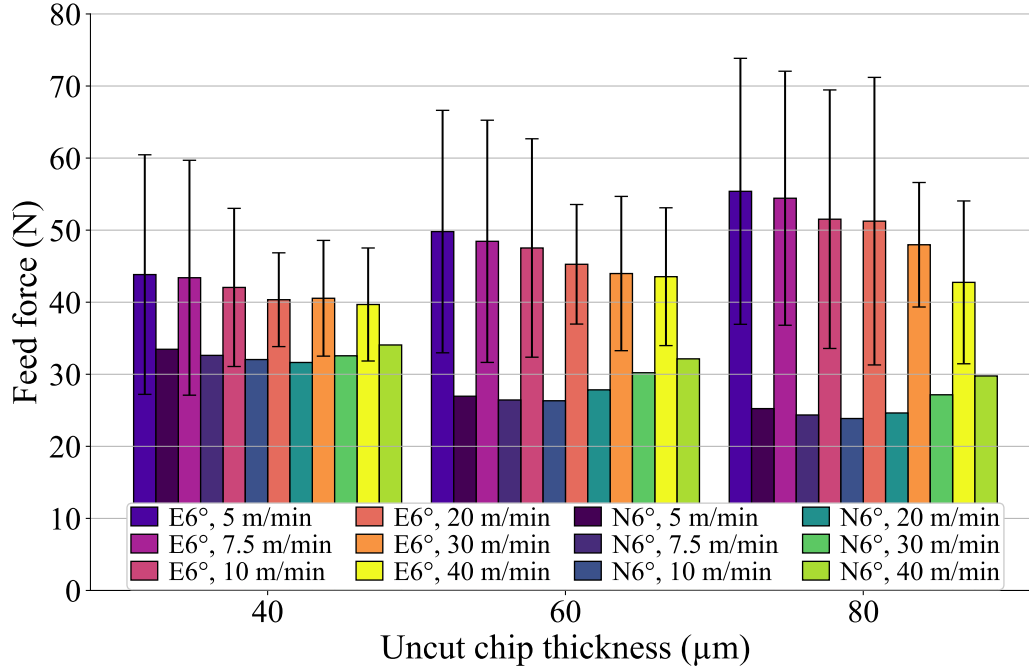


Figure 12: Comparison of experimental (E) and numerical (N) feed forces at the cutting edge inclination of 6° for the 3 uncut chip thicknesses (40, 60 and 80 μm) and the 6 cutting speeds (5, 7.5, 10, 20, 30 and 40 m/min)

Table 6: Synthetic overview of the results: differences between the experimental and the numerical results (mean difference for each cutting edge inclination, and maximal, minimal and mean differences for all the conditions) for the cutting force, ΔF_c , the feed force, ΔF_f , the passive force, ΔF_p , and the chip thickness ratio, $\Delta \lambda_h$

Difference	ΔF_c (%)	ΔF_f (%)	ΔF_p (%)	$\Delta \lambda_h$ (%)
Mean $\lambda_s = 0^\circ$	3	38	–	14
Mean $\lambda_s = 6^\circ$	4	40	26	21
Max global	10	60	29	38
Min global	1	10	19	2
Mean global	4	39	26	17

289 5. Conclusions

290 In this paper, an experimental study has been carried out in free orthogonal
291 and oblique cutting of the titanium alloy Ti6Al4V. It is a reference to assess the

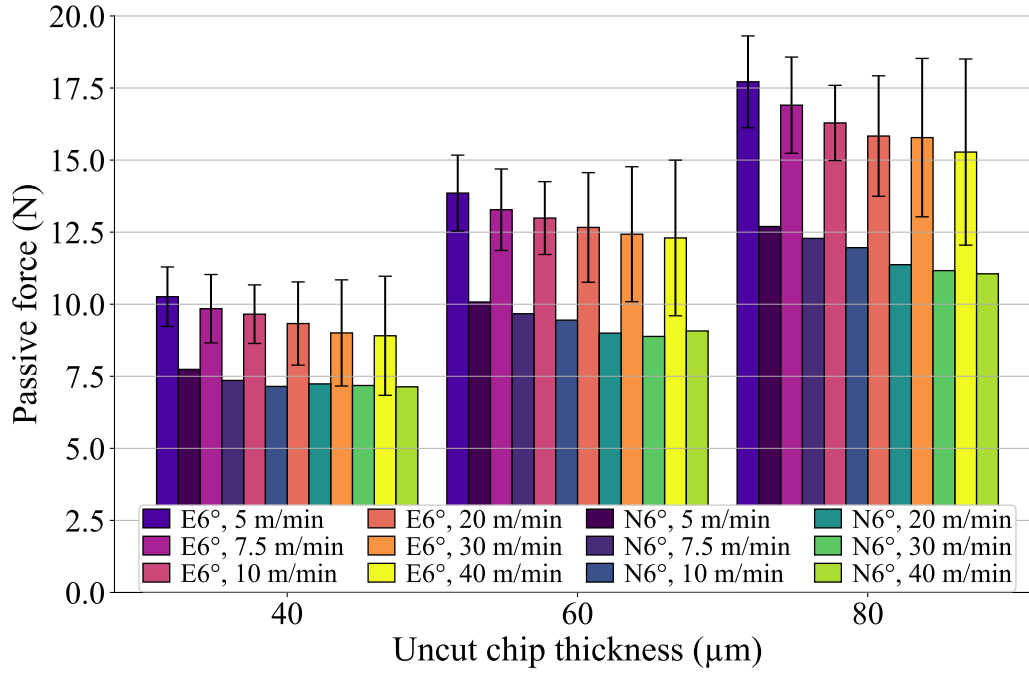


Figure 13: Comparison of experimental (E) and numerical (N) passive forces at the cutting edge inclination of 6° for the 3 uncut chip thicknesses (40, 60 and 80 μm) and the 6 cutting speeds (5, 7.5, 10, 20, 30 and 40 m/min)

292 performances of the 3D FE model introducing an ANN-based constitutive model
 293 and developed in the same conditions. An unpreviously seen wide range of cut-
 294 ting conditions, 36, is considered, including 2 cutting edge inclinations. Accurate
 295 evaluation of fundamental variables in 3D with the absence of tuning of both nu-
 296 merical parameters and model features when cutting conditions and inclination
 297 angle are significantly modified is a strong novelty of this work. Only chang-
 298 ing the inclination angle to move from free orthogonal to oblique cutting while
 299 maintaining the quality of the results has no equivalent in the current literature,
 300 moreover as no study on free oblique cutting is available. Predictive abilities of
 301 the model make it adequate for development of tools with a straight cutting edge,
 302 for example, providing the modelling of the feed force is improved if it is relevant
 303 for the study. This work moreover demonstrates the ability to model materials
 304 behaviour with ANN and opens possibilities in this promising direction.

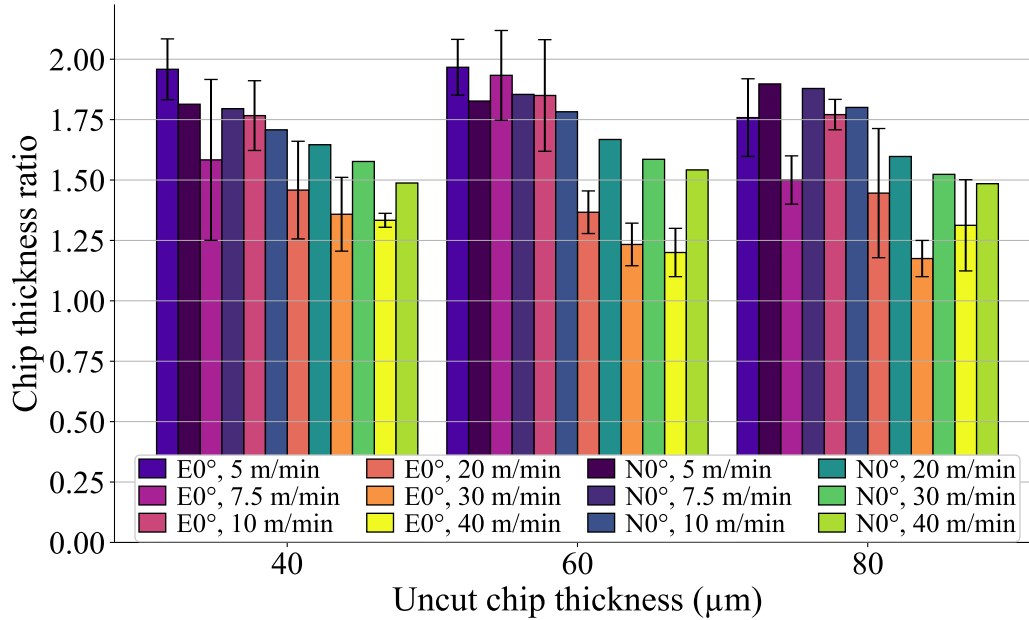


Figure 14: Comparison of experimental (E) and numerical (N) chip thickness ratios at the cutting edge inclination of 0° for the 3 uncut chip thicknesses (40, 60 and 80 μm) and the 6 cutting speeds (5, 7.5, 10, 20, 30 and 40 m/min)

References

- [1] P. J. Arrazola, T. Özel, D. Umbrello, M. Davies, I. S. Jawahir, Recent advances in modelling of metal machining processes, *CIRP Annals* 62 (2013) 695–718.
- [2] M. Agmell, V. Bushlya, S. V. A. Laakso, A. Ahadi, J.-E. Ståhl, Development of a simulation model to study tool loads in pcBN when machining AISI 316L, *Int J Adv Manuf Technol* 96 (2018) 2853–2865.
- [3] X. Xu, J. Outeiro, J. Zhang, B. Li, W. Zhao, Simulation of material side flow using a 3D coupled Eulerian-Lagrangian approach and a constitutive model considering the stress state, *Procedia CIRP* 102 (2021) 441–446.
- [4] M. Abouridouane, T. Bergs, D. Schraknepper, G. Wirtz, Friction behavior in metal cutting: Modeling and simulation, *Procedia CIRP* 102 (2021) 405–410.

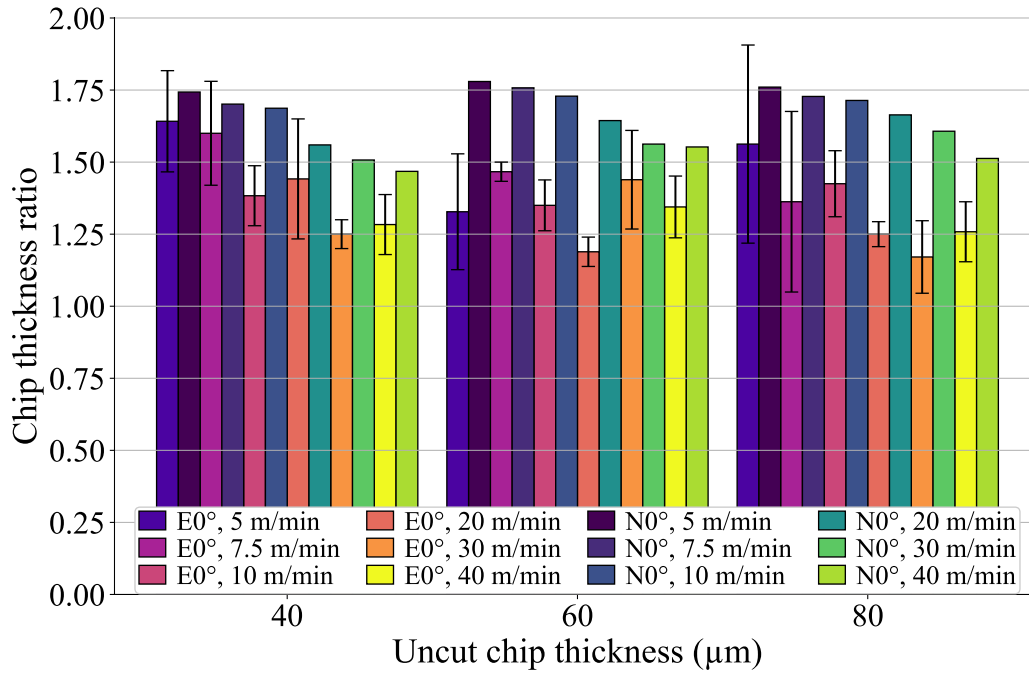


Figure 15: Comparison of experimental (E) and numerical (N) chip thickness ratios at the cutting edge inclination of 6° for the 3 uncut chip thicknesses (40, 60 and 80 μm) and the 6 cutting speeds (5, 7.5, 10, 20, 30 and 40 m/min)

- 318 [5] F. Ducobu, E. Rivière-Lorphèvre, E. Filippi, Experimental contribution to
 319 the study of the Ti6Al4V chip formation in orthogonal cutting on a milling
 320 machine, *Int J Mater Form* 8 (2015) 455–468.
- 321 [6] A. Sela, G. Ortiz-de-Zarate, D. Soler, G. Germain, P. Aristimuño, P. J. Arra-
 322 zola, Measurement of plastic strain and plastic strain rate during orthogonal
 323 cutting for Ti-6Al-4V, *International Journal of Mechanical Sciences* 198
 324 (2021) 106397.
- 325 [7] M. Afrasiabi, J. Saelzer, S. Berger, I. Iovkov, H. Klippel, M. Röthlin,
 326 A. Zabel, D. Biermann, K. Wegener, A Numerical-Experimental Study on
 327 Orthogonal Cutting of AISI 1045 Steel and Ti6Al4V Alloy: SPH and FEM
 328 Modeling with Newly Identified Friction Coefficients, *Metals* 11 (2021)
 329 1683.
- 330 [8] F. Ducobu, E. Rivière-Lorphèvre, E. Filippi, Application of the Coupled

- 331 Eulerian-Lagrangian (CEL) method to the modeling of orthogonal cutting,
332 Eur J Mech A Solids 59 (2016) 58–66.
- 333 [9] F. Ducobu, E. Rivière-Lorphèvre, E. Filippi, Finite element modelling of 3D
334 orthogonal cutting experimental tests with the Coupled Eulerian-Lagrangian
335 (CEL) formulation, Finite Elements in Analysis and Design 134 (2017) 27–
336 40.
- 337 [10] D. Ambrosio, A. Tongne, V. Wagner, G. Dessein, O. Cahuc, A new damage
338 evolution criterion for the coupled Eulerian-Lagrangian approach: Applica-
339 tion to three-dimensional numerical simulation of segmented chip formation
340 mechanisms in orthogonal cutting, Journal of Manufacturing Processes 73
341 (2022) 149–163.
- 342 [11] A. Vovk, J. Sölter, B. Karpuschewski, Finite element simulations of the
343 material loads and residual stresses in milling utilizing the CEL method,
344 Procedia CIRP 87 (2020) 539–544.
- 345 [12] M. Hardt, T. Bergs, Three Dimensional Numerical Modeling of Face Turn-
346 ing Using the Coupled-Eulerian-Lagrangian Formulation, Procedia CIRP
347 102 (2021) 162–167.
- 348 [13] S. N. Melkote, W. Grzesik, J. Outeiro, J. Rech, V. Schulze, H. Attia, P.-J.
349 Arrazola, R. M’Saoubi, C. Saldana, Advances in material and friction data
350 for modelling of metal machining, CIRP Annals 66 (2017) 731–754.
- 351 [14] G. Johnson, W. Cook, A constitutive model and data for metals subjected
352 to large strains, high strain rates and high temperatures, in: Proc. 7th Inter-
353 national Symposium on Ballistics, volume 21, The Hague, The Netherlands,
354 pp. 541–547.
- 355 [15] M. Calamaz, D. Coupard, F. Girot, A new material model for 2D numer-
356 ical simulation of serrated chip formation when machining titanium alloy
357 Ti–6Al–4V, International Journal of Machine Tools and Manufacture 48
358 (2008) 275–288.
- 359 [16] T. Özel, T. Altan, Determination of workpiece flow stress and friction at the
360 chip–tool contact for high-speed cutting, Int J Mach Tools Manuf 40 (2000)
361 133–152.

- 362 [17] A. Shrot, M. Bäker, Determination of Johnson–Cook parameters from ma-
363 chining simulations, *Comput Mater Sci* 52 (2012) 298–304.
- 364 [18] F. Klocke, D. Lung, S. Buchkremer, I. S. Jawahir, From Orthogonal Cutting
365 Experiments towards Easy-to-Implement and Accurate Flow Stress Data,
366 *Materials and Manufacturing Processes* 28 (2013) 1222–1227.
- 367 [19] P. Bosetti, C. Maximiliano Giorgio Bort, S. Bruschi, Identification of John-
368 son–Cook and Tresca’s Parameters for Numerical Modeling of AISI-304
369 Machining Processes, *J Manuf Sci Eng* 135 (2013).
- 370 [20] B. Denkena, T. Grove, M. A. Dittrich, D. Niederwestberg, M. Lahres, In-
371 verse Determination of Constitutive Equations and Cutting Force Modelling
372 for Complex Tools Using Oxley’s Predictive Machining Theory, *Procedia*
373 *CIRP* 31 (2015) 405–410.
- 374 [21] T. Bergs, M. Hardt, D. Schraknepper, Determination of Johnson-Cook ma-
375 terial model parameters for AISI 1045 from orthogonal cutting tests using
376 the Downhill-Simplex algorithm, *Procedia Manuf* 48 (2020) 541–552.
- 377 [22] M. Hardt, D. Schraknepper, T. Bergs, Investigations on the Application of
378 the Downhill-Simplex-Algorithm to the Inverse Determination of Material
379 Model Parameters for FE-Machining Simulations, *Simulation Modelling*
380 *Practice and Theory* 107 (2021) 102214.
- 381 [23] B. Stampfer, G. González, E. Segebade, M. Gerstenmeyer, V. Schulze, Ma-
382 terial parameter optimization for orthogonal cutting simulations of AISI4140
383 at various tempering conditions, *Procedia CIRP* 102 (2021) 198–203.
- 384 [24] M. Hardt, D. Jayaramaiah, T. Bergs, On the Application of the Particle
385 Swarm Optimization to the Inverse Determination of Material Model Pa-
386 rameters for Cutting Simulations, *Modelling* 2 (2021) 129–148.
- 387 [25] N. Kugalur Palanisamy, E. Rivière Lorphèvre, M. Gobert, G. Briffoteaux,
388 D. Tuytens, P.-J. Arrazola, F. Ducobu, Identification of the Parameter Val-
389 ues of the Constitutive and Friction Models in Machining Using EGO Algo-
390 rithm: Application to Ti6Al4V, *Metals* 12 (2022) 976.
- 391 [26] O. Pantalé, P. Tize Mha, A. Tongne, Efficient implementation of non-linear
392 flow law using neural network into the Abaqus Explicit FEM code, *Finite*
393 *Elements in Analysis and Design* 198 (2022) 103647.

- [27] S. Seo, O. Min, H. Yang, Constitutive equation for Ti–6Al–4V at high temperatures measured using the SHPB technique, *Int J Impact Eng* 31 (2005) 735–754.
- [28] F. Ducobu, E. Rivière-Lorphèvre, E. Filippi, On the importance of the choice of the parameters of the Johnson-Cook constitutive model and their influence on the results of a Ti6Al4V orthogonal cutting model, *Int J Mech Sci* 122 (2017) 143–155.
- [29] GRANTA EduPack 2020, Granta Design Limited, 2020.
- [30] N. Milošević, I. Aleksic, Thermophysical properties of solid phase Ti-6Al-4V alloy over a wide temperature range (2012).
- [31] J. Rech, P. J. Arrazola, C. Claudin, C. Courbon, F. Pusavec, J. Kopac, Characterisation of friction and heat partition coefficients at the tool-work material interface in cutting, *CIRP Annals* 62 (2013) 79–82.
- [32] O. Pantalé, Coefficients of an ANN constitutive flow law of a Ti6-Al-4V material for dynamic applications, Zenodo (2022).
- [33] L. Wang, H. Long, Investigation of material deformation in multi-pass conventional metal spinning, *Materials & Design* 32 (2011) 2891–2899.
- [34] F. Ducobu, E. Rivière-Lorphèvre, E. Filippi, On the introduction of adaptive mass scaling in a finite element model of Ti6Al4V orthogonal cutting, *Simulation Modelling Practice and Theory* 53 (2015) 1–14.

Appendix A. Coefficients of the ANN 3-9-7-1-sig

In this Appendix, we present the values obtained after the training phase of an ANN containing 9 neurons in the first hidden layer and 7 neurons in the second hidden layer.

The training of the neural network was performed using a data set containing 3 430 data points defined by:

- 70 values for $\varepsilon^p \in [0.0, 3.0]$, so that $[\varepsilon^p]_{min} = 0$ and $[\varepsilon^p]_{max} = 3$.
- 7 plastic strain rates $\dot{\varepsilon}^p \in [1, 10, 50, 500, 5\,000, 50\,000, 500\,000]$, so that $[\ln(\dot{\varepsilon}^p)]_{min} = 0$ and $[\ln(\dot{\varepsilon}^p)]_{max} = 13.12236$. [FD:] Add units to values?

423 • 7 temperatures $T \in [293, 400, 500, 700, 900, 1\,200, 1\,500]$, so that $[T]_{min} =$
 424 293 and $[T]_{max} = 1\,500$. [FD:] Add units to values?

425 Stresses in the training dataset ranges from $[\sigma^y]_{min} = 171.44$ to $[\sigma^y]_{max} =$
 426 2606.12. The results of the training process are given below for quantities \mathbf{W}_1 ,
 427 \mathbf{W}_2 , \vec{w} , \vec{b}_1 , \vec{b}_2 and b .

$$\mathbf{W}_1 = \begin{bmatrix} -0.87229 & -0.47675 & -1.50771 \\ -0.95762 & -0.25619 & 1.65222 \\ -10.61660 & 0.22003 & -0.11539 \\ 3.67883 & 0.37146 & -1.51069 \\ -63.39468 & 0.15466 & -0.95431 \\ 0.54807 & 0.25959 & -5.44355 \\ -1.33883 & 0.36089 & -1.66735 \\ -0.68125 & 1.02121 & 0.34242 \\ 0.08740 & 0.18764 & -41.32542 \end{bmatrix}$$

$$\mathbf{W}_2^T = \begin{bmatrix} 1.66285 & -0.59645 & -3.17333 & 0.20706 & 1.18760 & 2.01250 & -0.82147 \\ -0.26237 & -2.50330 & -1.45941 & -1.59833 & 4.05169 & -1.21146 & 1.05610 \\ -0.12958 & 0.67119 & -5.85989 & -2.55061 & 4.85245 & 4.31876 & 3.24070 \\ -2.12890 & 0.68296 & 0.71183 & 0.81706 & -0.09405 & 0.34919 & -1.41223 \\ 2.33631 & -0.08089 & 14.65789 & 0.12531 & 23.66363 & 2.55872 & 2.15338 \\ 0.11567 & 1.77629 & -1.80448 & 0.77825 & -1.58254 & 1.90442 & 1.23152 \\ 1.49265 & 0.41821 & -3.53803 & -0.48705 & -0.23671 & 0.75887 & -0.37441 \\ 0.95990 & 0.69041 & 0.43870 & 0.28393 & -1.40101 & -0.64569 & -0.38964 \\ 5.89937 & -0.13015 & 2.99264 & 1.78534 & -3.90189 & 1.17494 & -3.78854 \end{bmatrix}$$

$$\vec{w} = \begin{bmatrix} 0.34701 \\ 1.42079 \\ -0.96564 \\ 0.62467 \\ -0.56322 \\ 0.40960 \\ -0.42810 \end{bmatrix}$$

$$\vec{b}_1 = \begin{bmatrix} 2.57141 \\ 0.22673 \\ -1.16985 \\ -0.11246 \\ -0.82210 \\ -2.13264 \\ 0.78794 \\ 1.20434 \\ -3.48681 \end{bmatrix}$$

$$\vec{b}_2 = \begin{bmatrix} -0.36566 \\ -1.14445 \\ -0.79065 \\ -0.50670 \\ 1.30136 \\ 0.04521 \\ -0.29995 \end{bmatrix}$$

$$b = 0.04213$$